# A third-order multistep time discretization for a Chebyshev tau spectral method

A.W. Vreman[a], J.G.M. Kuerten[b,c]

[a]*AkzoNobel, Research Development & Innovation, Process Technology, P.O. Box 10, 7400 AA Deventer, The Netherlands*
[b]*Department of Mechanical Engineering, Eindhoven University of Technology, P.O. Box 513, 5600 MB Eindhoven, The Netherlands*
[c]*Faculty EEMCS, University of Twente, P.O. Box 217, 7500 AE Enschede, The Netherlands*

## Abstract

A time discretization scheme based on the third-order backward difference formula has been embedded into a Chebyshev tau spectral method for the Navier-Stokes equations. The time discretization is a variant of the second-order backward scheme proposed by Krasnov *et al.* (J. Fluid Mech., 2008). High-resolution direct numerical simulations of turbulent incompressible channel flow have been performed to compare the backward scheme to the Runge-Kutta scheme proposed by Spalart *et al.* (J. Comp. Phys., 1991). It is shown that the Runge-Kutta scheme leads to a poor convergence of some third-order spatial derivatives in the direct vicinity of the wall, derivatives that represent the diffusion of wall-tangential vorticity. The convergence at the wall is shown to be significantly improved if the backward scheme is applied.

*Keywords:* Chebyshev tau method, multistep time discretization, Navier-Stokes equations, DNS of turbulent channel flow

## 1. Introduction

In recent direct numerical simulations of turbulent channel flow with a spectral Chebyshev tau method, we noticed large errors in the budgets of the turbulence dissipation rate and enstrophy in the direct vicinity of the wall [1]. The time discretization scheme used was the Runge-Kutta method proposed by Spalart *et al.* [2], which is third-order accurate for the convective and second-order accurate for the viscous terms. Fortunately, these errors did apparently not affect the accuracy of quantities outside the direct vicinity of the wall, nor did they affect any mean value or standard deviation of a quantity based on the velocity or on spatial velocity derivatives up to order two. Nonetheless, the occurrence of these errors is disconcerting for a method which is regarded as one of the most accurate for direct numerical simulation of turbulent channel flow. The purpose of this note is to investigate this issue in more detail. It will appear that the issue is not resolved by spatial refinement if the time discretization method is not changed. We will therefore formulate and test an alternative time discretization method, which has at least the same formal order of accuracy as the Runge-Kutta method mentioned. It is a third-order variant of the second-order backward method proposed by Krasnov *et al.* [3].

## 2. A third-order time discretization scheme

The Chebyshev tau spectral method considered is based on the equation of the wall-normal component of the vorticity and the equation of the Laplacian of the wall-normal component of the velocity and has frequently been used in direct numerical simulation (DNS) of turbulent channel flow [4, 5, 6, 7, 8, 3, 9, 10, 11, 12, 13, 1]. Only the wall-normal direction is treated with the Chebyshev tau discretization; the periodic streamwise and spanwise directions are treated with the Fourier spectral discretization [18, 19].

---

*Email address:* `bert.vreman@akzonobel.com` (A.W. Vreman)

Although the pressure has been eliminated from the equations, this Chebyshev tau method requires, like pressure-based Chebyshev methods [14, 15, 16, 17], a type of influence matrix (Green's functions) technique for the enforcement of the correct wall boundary conditions.

In the first DNS of turbulent channel flow [4], this Chebyshev tau method was used in combination with the second-order accurate Crank-Nicolson Adams-Bashforth time discretization method (CN-AB). Later on, the Runge-Kutta method proposed by Spalart *et al.* [2], referred to as RK, was often used in spectral DNS of turbulent channel flow, see for example Refs. [5, 6, 7, 8, 11, 12, 13, 1]. Compared to CN-AB, the advantages of RK are that it is self-starting and third-order accurate for the convective terms. Krasnov *et al.* [3] and others [9, 10] combined the (pressureless) Chebyshev tau method with a time discretization scheme based on the second-order backward finite difference formula. However, these references do not clarify why this scheme was used instead of CN-AB or RK, which is more accurate for the convective terms. Since we prefer that an alternative to RK is at least third-order accurate for convective terms, we will introduce a third-order variant of the backward scheme of Krasnov *et al.* [3] in the following. We call this scheme B3.

The Chebyshev tau method considered is based on the evolution equations for four primary variables, two three-dimensional variables and two one-dimensional variables. The two three-dimensional primary variables are the wall-normal component of the vorticity ($\omega_2$) and the Laplacian of the wall-normal component of the velocity ($\phi = \Delta u_2$). The two one-dimensional primary variables are $U_1$ and $U_3$, the streamwise and spanwise velocity components averaged over the streamwise and spanwise directions. The third-order backward discretization of the four evolution equations can be written in the form,

$$\frac{11\hat{g}^{n+1} - 18\hat{g}^n + 9\hat{g}^{n-1} - 2\hat{g}^{n-2}}{6\,\delta t} = \nu \hat{L}\hat{g}^{n+1} + \hat{F}_g\left(\hat{\omega}_2^*, \hat{\phi}^*, \hat{U}_1^*, \hat{U}_3^*\right), \tag{1}$$

where the time-level is denoted in superscript and $\delta t$ is the time-step. The symbol $\hat{g}$ stands for the spectral transforms of $\omega_2$, $\phi$, $U_1$ and $U_2$. In addition, $\hat{L}$ denotes the spectral representation of the Laplace operator, $\nu$ the kinematic viscosity, and $\hat{F}_g$ denotes the nonlinear operator that expresses the non-viscous terms into the primary variables. The asterisk superscript indicates that the variable is extrapolated to time level $n+1$ using the third-order extrapolation formula,

$$\hat{q}^* = 3\hat{q}^n - 3\hat{q}^{n-1} + \hat{q}^{n-2}. \tag{2}$$

This completes the definition of time discretization scheme B3, which is formally third-order accurate for both convective and viscous terms. Apart from the order of accuracy, there are two other notable differences between scheme B3 and the second-order backward method of Krasnov *et al.* [3]. Whereas in Ref. [3] the linear extrapolation operator (2) is applied to nonlinear terms computed from non-extrapolated primary variables, in Eq. (1) the nonlinear operator is applied to extrapolated primary variables. The advantage of the latter is that no storage of nonlinear terms for reuse in future time steps is required. The primary variables do need to be stored, but this is required anyway, due to the left-hand side of Eq. (1). The second difference concerns the Von Neumann stability regime. Like scheme CN-AB, the second-order backward scheme is unstable in the inviscid limit, which means that the scheme is unstable on the entire imaginary axis, parametrized with $iy$ ($y$ is real), except if $y = 0$. However, scheme B3 is stable in the inviscid limit, since the stable region includes the interval $|y| < 0.63$. For comparison, the stable region of scheme RK includes the interval $|y| < 1.73$, almost three times larger, but the method is a three-stage method and therefore per time step three times as expensive as scheme B3. Due to the implicit treatment of the viscous terms, scheme B3 contains, like schemes CN-AB and RK, the entire left-half of the real axis.

Scheme RK is a low-storage scheme; the primary variables need only to be stored for the actual stage and the previous stage. In contrast, for scheme B3 the primary variables need to be stored for the actual time step and three previous time steps. Thus for the storage of primary variables scheme B3 requires twice as much memory as scheme RK. In our implementations, in which auxiliary variables are used for efficient computation of the dealiased nonlinear terms (based on $\mathbf{u} \times \boldsymbol{\omega}$), the total storage requirements for scheme B3 compared to scheme RK is much less higher than a factor of two.
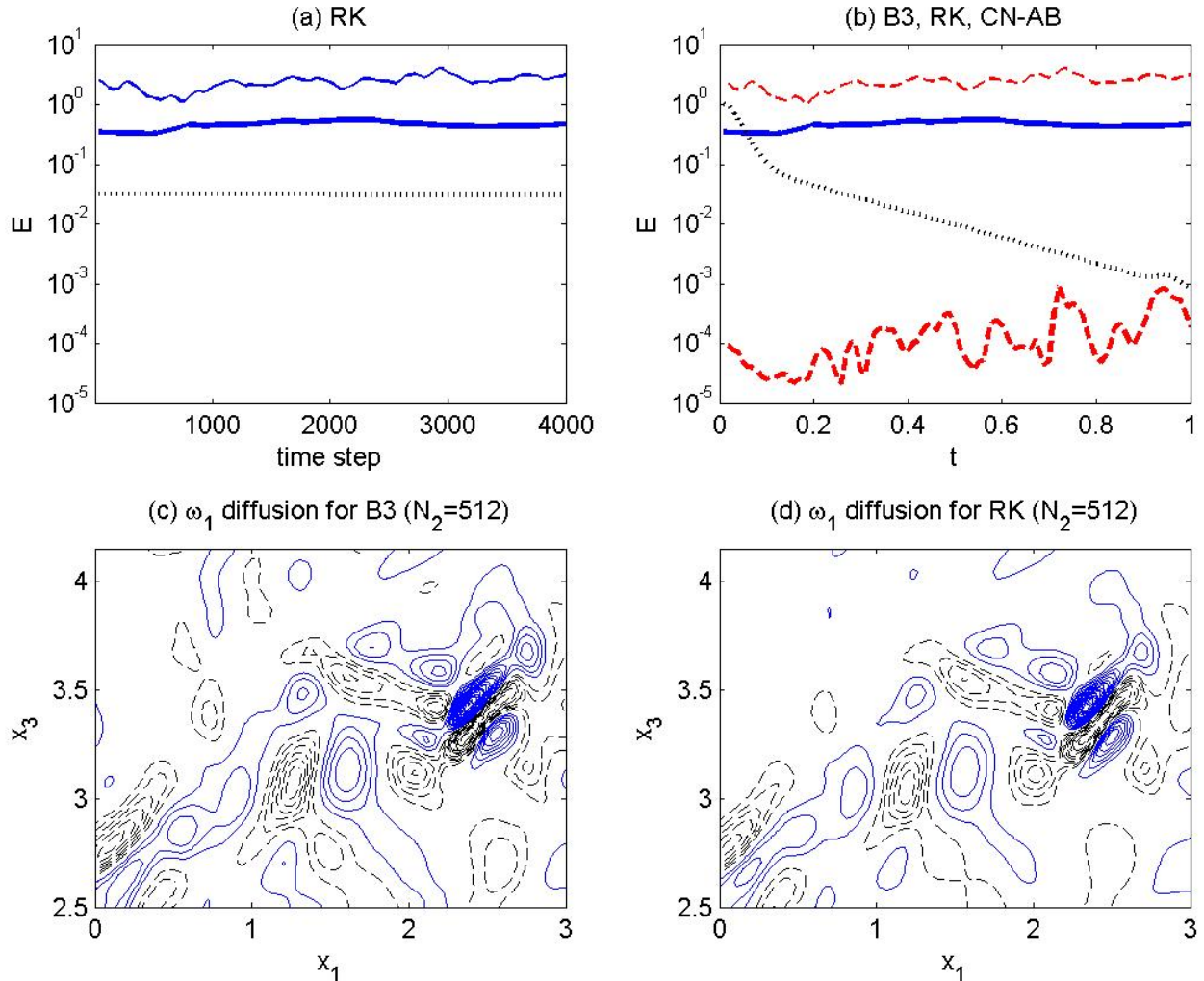
Figure 1: (a,b): Transient behaviour of $E$ (relative wall-error in discretized $\omega_1$ equation) for small domain simulations ($L = 2\pi$). (a): Thin blue solid: scheme RK, $N_2 = 192$, $\delta t = 2.5 \cdot 10^{-4}$; Thick blue solid: scheme RK, $N_2 = 512$, $\delta t = 2.5 \cdot 10^{-4}$; Thick black dotted: scheme RK, $N_2 = 512$, $\delta t = 2.5 \cdot 10^{-6}$. (b): Thin red dashed: scheme B3, $N_2 = 192$, $\delta t = (2.5 \cdot 10^{-4})/3$; Thick red dashed: scheme B3, $N_2 = 512$, $\delta t = (2.5 \cdot 10^{-4})/3$; Thick blue solid: scheme RK, $N_2 = 512$, $\delta t = 2.5 \cdot 10^{-4}$; Thick black dotted: scheme CN-AB, $N_2 = 512$, $\delta t = (2.5 \cdot 10^{-4})/3$. (c,d): Negative (solid) and positive (dashed) contours of $\nu\Delta\omega_1$ on part of a wall at $t = 1.01$ for two small domain simulations. The contour increment is 1000. (c): Scheme B3, $N_2 = 512$, $\delta t = 0.833 \cdot 10^{-4}$. (d): Same simulation shown as in (c), except that at $t = 1$ scheme B3 with $\delta t = (2.5 \cdot 10^{-4})/3$ was replaced by scheme RK with $\delta t = 2.5 \cdot 10^{-4}$.

## 3. Results

In the remainder of this note, we show how RK and B3 perform in high-resolution DNS of turbulent channel flow at $Re_\tau = 180$ (the channel half-width $H$ and the friction velocity $u_\tau$ are both equal to 1 and the kinematic viscosity $\nu$ is equal to 1/180). The flow is driven by a fixed mean streamwise pressure gradient. The streamwise, wall-normal and spanwise directions correspond to $x_1$, $x_2$ and $x_3$. These directions are discretized with $N_1$ Fourier modes, $N_2 + 1$ Chebyshev modes and $N_3$ Fourier modes, respectively. Nonlinear products are computed in physical space, with use of dealiasing in the $x_1$ and $x_3$ directions only (the grid in physical space contains $3N_1/2 \times (N_2 + 1) \times 3N_3/2$ points). The domain size is $L \times 2 \times L/3$. Statistics of the statistically steady state that will be shown have been obtained in the standard domain, $L = 4\pi$. The transient behaviour of the solution was studied in a smaller domain ($L = 2\pi$). The smaller domain size made it much more efficient to explore a large number of discretizations, grid sizes and error quantities.

In the discussion of the results, we focus on the vorticity equation. The $i$-component of the vorticity equation is given by,

$$\partial_t \omega_i = -\mathbf{u} \cdot \nabla \omega_i + \boldsymbol{\omega} \cdot \nabla u_i + \nu\Delta\omega_i, \qquad (3)$$

3

where $\boldsymbol{\omega}$ and $\mathbf{u}$ are the vorticity and velocity vectors, respectively. The Chebyshev tau spectral method under consideration is based on discretization of the equations for $\omega_2$ and $\phi = \Delta u_2$; the evolution equations for $\omega_1$ and $\omega_3$ are not discretized in this method. It is therefore particularly interesting to investigate to what extent the equations for $\omega_1$ and $\omega_3$ are satisfied by the numerical solution. If a unique smooth solution of the Navier-Stokes initial boundary value exists, then all equations derived from the Navier-Stokes equations should be satisfied by the numerical solution in the limit of zero grid size and zero time step.

To introduce Fig. 1, we briefly describe the definition of the simulations in the small domain. Each simulation shown in Fig. 1a and Fig. 1b was started from the same initial condition, which was a snapshot of a a fully turbulent field provided by a pre-simulation performed with scheme B3, $N_2 = 192$ and $N_1 = N_3 = 96$. Because the snapshot is in fact a finite collection of expansion coefficients of smooth basis functions, the initial condition represents a smooth (infinitely differentiable) velocity field that is divergence free within machine precision. For each case shown in Fig. 1, we post-processed the results to determine all terms of Eq. (3). The post-processing routine used for each case employed the Chebyshev tau spectral discretization for the terms at the right-hand side and the fourth-order backward difference formula for the time-derivative at the left-hand side (from several post-processing runs performed with the fourth-order central difference scheme, it is concluded that the effect of the particular time discretization scheme used to evaluate Eq. (3) is small, provided the time discretization is of sufficiently high order). It is remarked that Fig. 1a and Fig. 1b are restricted to the transient behaviour of the relative error of the streamwise component of the vorticity equation on the wall, which is defined by

$$E(t) = \|\partial_t \omega_1 - \nu \Delta \omega_1\| \ / \ \|\partial_t \omega_1\|, \tag{4}$$

where $\|.\|$ represents the discrete $L_2$-norm over the two wall planes. Since the no-slip boundary condition implies $\partial_t \omega_1 = \nu \Delta \omega_1$ on the walls, $E(t)$ should converge to zero for all times $t > 0$, if both grid size and time step converge to zero. In particular, for a high resolution spectral DNS, we would expect a very small value of $E(t)$ for $t > 0$.

Figure 1a shows results of three different simulations with scheme RK and $N_1 = N_3 = 96$. The first simulation was performed with $N_2 = 192$ and $\delta t = 2.5 \cdot 10^{-4}$. Although the grid size in plus units is smaller than standard [5] and as small as in the high resolution case in [13], $E(t)$ appears to be very large, $\|\nu \Delta \omega_1\|$ is mostly much larger than $\|\partial_t \omega_1\|$ (Fig. 1a). However, a spectral method is expected to show exponential convergence for sufficiently fine resolution. Thus a second simulation was performed with $N_2 = 512$ and $\delta t = 2.5 \cdot 10^{-4}$. Fig. 1a shows that although $E(t)$ has dropped compared to the first simulation, the relative error is still large, about 10%. In the third simulation shown in Fig. 1a, the time step was reduced, with a factor 100 ($N_2 = 512$) to obtain a reasonably low error (about 1%). However, a time step of $\delta t = 2.5 \cdot 10^{-6}$ is undesirably small for a long-time simulation. Assuming that the spatial resolution is sufficient in this case, we conclude from this (and a simulation at a time step $\delta t = 2.5 \cdot 10^{-5}$, not shown) that the convergence of the error to zero is roughly $O((\delta t)^{0.7})$, much slower than the formal order of accuracy of RK suggests. Only results of simulations without dealiasing in the normal direction are shown, but it has been verified that dealiasing in the wall-normal direction does not lead to a much smaller error. The same procedure can not be used to confirm the temporal order of accuracy for scheme B3, because compared to the simulation with scheme RK, the error $E$ in the simulation with scheme B3 on the same grid ($N_2 = 512$) is already very small for the largest time step (Fig. 1b). We found that reducing the time step for scheme B3 does not lead to significant further reduction of $E$, which indicates that in that case $E$ is not dominated by the temporal but by the spatial discretization.

Figure 1b shows results of two simulations performed with B3, one simulation performed with RK and one simulation performed with CN-AB. Each simulation used $N_1 = N_3 = 96$. The first simulation was performed with scheme B3, $N_2 = 192$ and $\delta t = (2.5 \cdot 10^{-4})/3$ (the first and second time steps were performed with the first-order and second-order variant of scheme B3, respectively). Fig. 1b shows that in this case the wall error $E$ is very large, like in the simulation with scheme RK on the same grid shown in Fig. 1a. The second simulation was also performed with scheme B3, but with much larger wall-normal resolution, $N_2 = 512$ ($\delta t = (2.5 \cdot 10^{-4})/3$). As a result, the error drops with roughly six orders of magnitude, clearly an indication of the exponential convergence we expect from a spectral method. The third simulation shown in Fig. 1b was performed with scheme RK, $N_2 = 512$ and $\delta t = 2.5 \cdot 10^{-4}$, a three times larger time step because RK is a three-stage method. It is the same curve as the second curve in

| Case | $N_1 \times N_2 \times N_3$ | Scheme | $4000\delta t$ | Statistical averaging time | Number of fields |
|------|------|------|------|------|------|
| S2-RK | $384 \times 192 \times 192$ | RK | 1 | 200 | 3200 |
| S2-B3 | $384 \times 192 \times 192$ | B3 | 1/3 | 200 | 3200 |
| S3-B3 | $384 \times 384 \times 192$ | B3 | 1/3 | 200 | 3200 |
| S4-B3 | $576 \times 576 \times 288$ | B3 | 2/9 | 100 | 1600 |

Table 1: Simulations in the standard domain, $L = 4\pi$. For each case the number of spectral modes, the time discretization scheme, the time step $\delta t$, the statistical averaging time and the number of fields used for the statistics are shown. Dealiasing was applied in the $x_1$- and the $x_3$-direction, *i.e.* the grid in physical space contained $(3N_1/2) \times (N_2 + 1) \times (3N_3/2)$ points.

Fig. 1a, and has been included to illustrate that in the direct vicinity of the wall the RK method leads to a surprisingly slow convergence of the numerical solution to the analytical solution of this Navier-Stokes problem (assuming that such an analytical smooth solution exists and is unique). The fourth simulation shown in Fig. 1b was performed with scheme CN-AB, $N_2 = 512$ and $\delta t = (2.5 \cdot 10^{-4})/3$ (in the first time-step the convective terms were treated with forward Euler). The behaviour of this case is also remarkable. In the first few time steps the relative wall error is very large, larger than in the simulation performed with RK. However, in this case the error gradually drops to the very low level of the error of the simulation performed with B3 and $N_2 = 512$ (the decline takes about 12000 time steps). We inspected the behaviour of $\nu\Delta\omega_1$ in a single point on the wall and found, on top of the physical signal, a slowly decaying spurious wave, which alternated each time step.

From the simulation with the smallest error in Fig. 1b (scheme B3, $N_2 = 512$, $\delta t = (2.5 \cdot 10^{-4})/3$), flow structures of the viscous diffusion of vorticity on (part) of a wall at $t = 1.01$ are shown in Fig. 1c. In addition, structures of a simulation that was identical except that at $t = 1$ the time stepping scheme B3 with $\delta t = (2.5 \cdot 10^{-4})/3$ was replaced by scheme RK with $\delta t = 2.5 \cdot 10^{-4}$ are shown in Fig. 1d. The differences are significant, both the maximum and the absolute mininum of the quantity on the wall reduced with about 20%, only by changing the time stepping scheme to RK. To verify that the differences between Fig. 1c and 1d can not be attributed to the chaotic behaviour of turbulence, the restart was repeated for B3 by treating $t = 1$ as a new initial condition, *i.e.* the first two time steps after $t = 1$ were performed with the first-order backward scheme and second-order backward scheme, respectively. This perturbation at $t = 1$ had negligible influence on the structures, the maximum and minimum of $\nu\Delta\omega_1$ on the wall at $t = 1.01$ were different by less than 0.1% instead of about 20%.

The question why scheme B3 appears to perform better than scheme RK is not easy to answer. To obtain further insight into the interaction between time discretization schemes and the Chebyshev tau method used in the simulations, we analyzed the theta method applied to the Chebyshev tau approximation of a representative Dirichlet problem in one-dimension. The theta method covers the treatment of the viscous terms for Runge-Kutta scheme RK, for scheme CN-AB (Crank-Nicolson, $\theta = 1/2$), and for backward Euler ($\theta = 1$), which is the single-step variant of scheme B3. In the Appendix, a theorem is proven, which states that $\lambda = -(1 - \theta)/\theta$ is an eigenvalue of the one-dimensional system. Thus if the theta method tends to the explicit side ($\theta < 1/2$), it is unconditionally unstable ($|\lambda| > 1$). In fact, the eigenvalue $\lambda$ is a spurious eigenvalue; it does not have a physical meaning, since it does not depend on viscosity and mode number, nor does it converge to 1 if $\delta t \to 0$. Only for the fully backward method ($\theta = 1$), the spurious eigenvalue is zero. The eigenvectors that correspond to $\lambda$ are the last two Chebyshev polynomials (order $N_2 - 1$ and $N_2$). It is tempting to set the coefficients of these two modes to zero at each time step in case $\theta < 1$. However, this is not a satisfactory remedy, because the solution will not satisfy the boundary conditions anymore. The Runge-Kutta method considered has three stages. In the first stage $\theta \approx 0.4336 < 1/2$ (then $\theta = \beta_1/(\alpha_1 + \beta_1)$, where $\alpha_1$ and $\beta_1$ are coefficients from page 323 of Ref. [2]). This is compensated by the other stages; the combined eigenvalue over three stages does not exceed one, such that RK is formally stable for linear systems. However, the nonlinear three-dimensional problem is much more complicated and it cannot be ruled out that an amplification in the first stage is somehow sustained by nonlinear effects. The Chebyshev tau spatial discretization leads to a very stiff system of ordinary differential equations, and backward time discretizations are known to work well for stiff systems.

The effect of the time discretization scheme on turbulence statistics has been investigated for the standard domain size ($L = 4\pi$). For this domain, four high-resolution direct numerical simulations
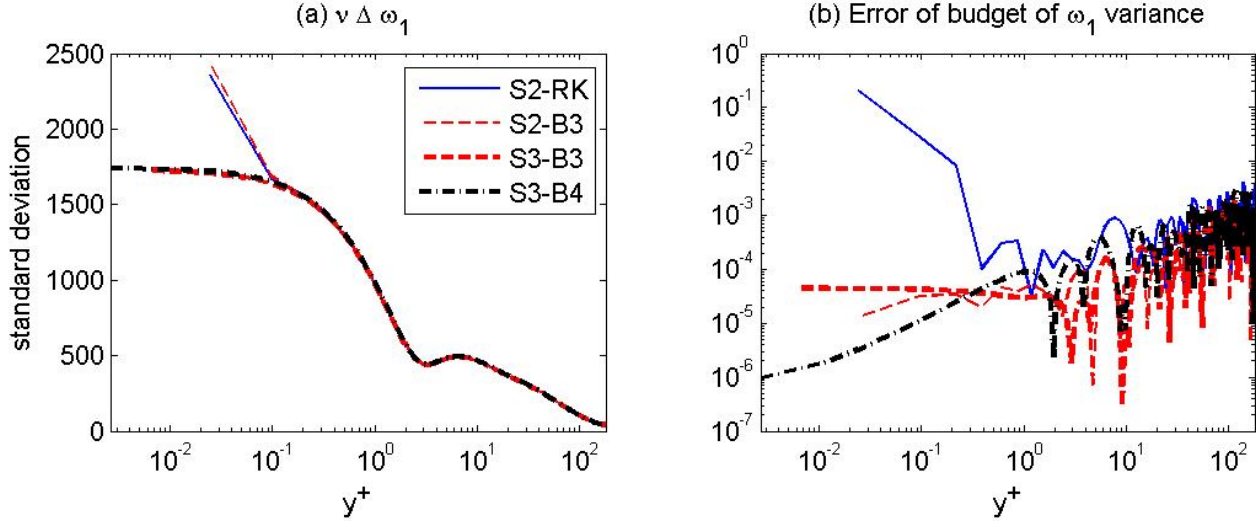
Figure 2: Statistical results for different cases in the domain with length $L = 4\pi$. Thin blue solid: S2-RK; Thin red dashed: S2-B3; Thick red dashed: S3-B3; Thick black dash-dotted: S4-B3. (a): Standard deviation of $\nu\Delta\omega_1$. (b): Relative error of the budget of the variance of $\omega_1$.

have been performed, one with scheme RK (simulation S2-RK), three with scheme B3 (simulations S2-B3, S3-B3 and S4-B3), see Table 1. Corresponding databases are available at www.vremanresearch.nl. Simulations S2-RK and S2-B3 were performed for $N_1 = 384$, $N_2 = N_3 = 192$. The time step was $2.5 \cdot 10^{-4}$ in case S2-RK and three times smaller in case S2-B3. As a refinement of case S2-B3, simulation S3-B3 was performed: $N_2 = 384$, while the other parameters were not changed. To check the grid independency of S3-B3, we performed simulation S4-B3, in which the resolution in space and time was increased with a factor 1.5 in each direction.

Figure 2a shows the profiles of the standard deviation (root mean square of the fluctuation) of the viscous term in the streamwise vorticity equation, $\nu\Delta\omega_1$, which represents the diffusion of streamwise vorticity. The coordinate $y^+$ is defined by $y^+ = Re_\tau(1 - |x_2|) = 180(1 - |x_2|)$ for $-1 \leq x_2 \leq 1$. The four profiles do not collapse in the region very close to the wall. Although the resolution in cases S2-RK and cases S2-B3 is more than standard, it is insufficient to capture the fluctuation of the Laplacian of the vorticity in the direct vicinity of the wall. However, this fluctuation is accurately captured by cases S3-B3 and S4-B3. We did not consider refinement of S2-RK on the large domain, since we concluded from the transient computations on the small domain that when scheme RK is used the error of the diffusion term of the streamwise vorticity remains large if the grid is refined, unless the time step is lowered to an extremely small value.

Figure 2b shows the error of the budget of the streamwise vorticity variance. The budget was obtained after multiplication of the fluctuation of the $\omega_1$ equation with the fluctuation of $\omega_1$ and subsequent time averaging. For more information about the derivation and physical meaning of this type of budgets, the reader is referred to Refs. [20, 21, 22, 1]. The curves in Fig. 2b have been normalized with the local value of the destruction term in the budget (this destruction term attains its maximum at the wall). The error of a budget is the sum of all terms in the budget. The error should reduce to zero if the time of statistical averaging is sufficiently long and the grid size and time step are sufficiently small. Figure 2b shows a small error of the budget in all cases with scheme B3, but a large error in case S2-RK in the region very close to the wall, which is due to a large error of the viscous diffusion term in the budget.

Fig. 2a shows that the near-wall error of the viscous term in the $\omega_1$ equation is large in cases S2-RK and S2-B3 (the maximum of the standard deviation of the viscous term, which is attained on the wall, is roughly four times larger than the maximum of the standard deviation of the vortex stretching term and only two times smaller than the maximum of the standard deviation of the convective term). Contour plots of the structures of the diffusion of streamwise wall vorticty on the wall ($\nu\Delta\omega_1$) have also been inspected. In case S3-B3 the structures of diffusion of streamwise wall vorticity were smooth, while in cases S2-B3 and S2-RK these structures were clearly under-resolved, showing peak values 10 times higher

6

than in case S3-B3. However, in case S2-B3 the large errors of this viscous term do not show up in the budget of the variance of $\omega_1$. This illustrates that a small budget error does not necessarily imply that all terms of the underlying instantaneous equation are accurate. For conciseness of this note, we showed results for the streamwise vorticity equation only, but the conclusions drawn from Fig. 1 and 2 also hold for the spanwise vorticity equation.

There have been speculations about the regularity of particular terms near the wall, prompted by the observation of increasing and diverging flatness (intermittency) of the normal velocity component near the wall with increasing resolution [23]. The present simulations do not support these speculations. The flatness of the normal velocity component at the first point off the wall is 29.2 for S2-RK, 27.7 for S2-B3, 29.8 for S3-B3 and 28.3 for S4-B3. Although the statistical averaging times are large, we can not rule out that the variation among the four cases is caused by statistical error, since this particular quantity is related to rare events in the viscous sublayer [24, 13].

## 4. Conclusions

In summary, we tested a multi-stage Runge-Kutta method and a third-order multi-step backward time discretization schemes in high-resolution DNS of turbulent channel flow at $Re_\tau = 180$. The time discretizations were embedded into a Chebyshev tau method based on evolution equations for the wall-normal component of the vorticity equation and the wall-normal component of the velocity Laplacian. For 192 Chebyshev modes in the wall-normal direction, both schemes produced large near-wall errors of the Laplacians of the tangential vorticity components. In case of the Runge-Kutta method these errors were accompanied by large near-wall errors of the budgets of the tangential vorticity variances. Fortunately, all these errors were only observed in the direct vicinity of the wall ($y^+ < 0.2$). It was verified that the near-wall errors do not deteriorate the accuracy of mean and standard deviation of the velocity, velocity gradient, pressure and pressure gradient, nor the accuracy of mean and standard deviations of the second-order spatial velocity derivatives. In addition, flow structures expressed in terms of the velocity and velocity gradient (which includes vorticity) are not affected. However, the structures of vorticity diffusion are affected at the wall. Surprisingly, for the Runge-Kutta method the near wall errors of the Laplacians of the tangential vorticity components did not reduce when only the spatial resolution was refined, while the convergence was less than first order in the time step when both temporal and spatial resolution were refined. However, for the third-order backward scheme the near-wall errors were found to drop by more than six orders of magnitude when the number of Chebyshev modes in the wall-normal direction was increased to 512, while the time-step remained the same. This observation is a numerical indication for the unproven but theoretically very important hypothesis that solutions of the Navier-Stokes equations on a wall bounded domain obey a high degree of regularity.

Finally, it is noted that the third-order multi-step backward time discretization proposed is not restricted to the Chebyshev tau method or the Navier-Stokes equations; the scheme may also be valuable for other spatial discretizations and other nonlinear convection-diffusion equations.

**Appendix: Stability analysis**

We consider the following simplified one-dimensional system [18] for two even variables $\phi(y, t)$ and $v(y, t)$ on the spatial interval $[-1, 1]$:

$$\partial_t \phi = \nu \phi_{,yy}, \tag{5}$$

$$v_{,yy} = \phi, \tag{6}$$

with even boundary conditions,

$$v = 0 \quad \text{and} \quad v_{,y} = 0, \quad \text{if} \quad y = \pm 1, \tag{7}$$

7

and even initial condition.

In the following we present the discrete version of this system, using the Chebyshev tau method in space and the single-step $\theta$-method in time. We prove that $-(1-\theta)/\theta$ is an eigenvalue of the discrete system. Let $M$ be the number of even Chebyshev polynomials taken into account, which means that we use the even Chebyshev polynomials of order up to $2M-2$. The spectral coefficients at time level $n$ are defined by the $M$-dimensional vectors $\hat{\phi}^n$ and $\hat{v}^n$. More precisely, $\hat{\phi}^n$ is in this subsection defined as the vector $[\hat{\phi}_0^n \ \hat{\phi}_2^n \ \hat{\phi}_4^n \ ... \ \hat{\phi}_{2M-2}^n]^T$, where $T$ denotes the transpose operator. We define the $M \times M$ second-order derivative Chebyshev matrix $D$, which is an upper triangular matrix with a zero diagonal. The nonzero coefficients are given by $D_{kj} = 4(j-1)^3$ if $j > k = 1$, and $D_{kj} = 8(j-1)((j-1)^2 - (k-1)^2)$ if $j > k > 1$.

In order to satisfy the boundary conditions on the new time level, we define

$$
\begin{align}
\hat{\phi}^{n+1} &= \hat{\phi}^* + c_e \phi^e, \tag{8}\\
\hat{v}^{n+1} &= \hat{v}^* + c_e \hat{v}^e, \tag{9}
\end{align}
$$

where $\phi^*$ and $v^*$ represent the solution of the system with homogenous Dirichlet boundary conditions, $\phi^* = v^* = 0$ at $y = \pm 1$, while $\phi^e$ and $v^e$ represent the particular solution of the system with even inhomogeneous Dirichlet boundary conditions, $\phi^e = 1$ and $v = 0$ at $y = \pm 1$. Since the variables are even, the boundary conditions imply

$$
\sum_{k=0}^{M-1} \hat{\phi}_{2k}^* = 0, \qquad \sum_{k=0}^{M-1} \hat{v}_{2k}^* = 0. \tag{10}
$$

In order to incorporate these boundary conditions into the matrix notation, we define the $M \times M$ matrix $Z$, which is zero except for the last row, in which all $M$ coefficients equal 1. In addition we define the unity matrix $I$, in which all elements are zero, except the $M$ diagonal coefficients, which are one. Furthermore, we define a pseudo-unity matrix $J$, which is equal to $I$ except that the last diagonal element is zero, $J_{MM} = 0$.

Above definitions are used to formulate a matrix representation for the discretization of the intermediate problem, which obeys homogeneous Dirichlet boundary conditions for both variables:

$$
\begin{align}
P\hat{\phi}^* &= Q\hat{\phi}^n, \tag{11}\\
R\hat{v}^* &= J\hat{\phi}^*, \tag{12}
\end{align}
$$

where $P = J - \theta\nu\delta tD + Z$, $Q = J + (1-\theta)\nu\delta tD$, and $R = D + Z$. In Eq. (11), and similarly in Eq. (12), the first $M-1$ rows of represent the discretization of the differential equation, while the last row represents the homogeneous Dirichlet boundary conditions. It is remarked that the last row of $D$ is zero by definition.

To impose the correct boundary conditions, we use the particular solutions $\hat{\phi}^e$ and $\hat{v}^e$ of the following systems,

$$
\begin{align}
P\hat{\phi}^e &= \hat{r}, \tag{13}\\
R\hat{v}^e &= J\hat{\phi}^e, \tag{14}
\end{align}
$$

where $\hat{r}$ is a vector that is zero except for the last element. The last element of $\hat{r}$ equals 1, which is the value of the Dirichlet boundary condition for $\phi^e$. The coefficient $c_e$ is determined by the requirement that $v^{n+1}$ should not only satisfy $v = 0$ at $y = \pm 1$, but also $v_{,y} = 0$ at $y = \pm 1$. For even $v$ the latter bounday condition is expressed by the condition

$$
d^T \hat{v}^{n+1} = 0, \tag{15}
$$

where coefficient $d_k$ of the vector $d$ is given by $d_k = 4(k-1)^2$, for $k = 1, 2, ... , M$. Substitution of Eq. (9) into Eq. (15) leads to the expression for the coefficient $c_e$:

$$
c_e = -\frac{d^T \hat{v}^*}{d^T \hat{v}^e}. \tag{16}
$$

The contribution of the particular solution to $\hat{\phi}^{n+1}$ can be written as

$$c_e \hat{\phi}^e = -\frac{1}{d^T \hat{v}^e} \hat{\phi}^e (d^T \hat{v}^*) = -\frac{1}{d^T \hat{v}^e} (\hat{\phi}^e d^T) \hat{v}^* = C\hat{v}^*, \tag{17}$$

where

$$C = -\frac{1}{d^T \hat{v}^e} \hat{\phi}^e d^T, \tag{18}$$

which is an $M \times M$ matrix.

Substitution of the definitions and derivations above into Eq. (8) implies that one time step can be written as

$$\hat{\phi}^{n+1} = \hat{\phi}^* + C\hat{v}^* = \hat{\phi}^* + C\hat{R}^{-1}J\hat{\phi}^* = (I + CR^{-1}J)P^{-1}Q\hat{\phi}^n, \tag{19}$$

or

$$\hat{\phi}^{n+1} = A\hat{\phi}^n, \quad \text{where} \quad A = (I + CR^{-1}J)P^{-1}Q. \tag{20}$$

**Theorem.** $\lambda = -(1-\theta)/\theta$ is an eigenvalue of the matrix $A$, and $\hat{r}$ is an eigenvector for this eigenvalue.

**Proof.** We start with the reminder that $\hat{r}$ is zero apart from the last element, which equals 1. We define $\lambda = -(1-\theta)/\theta$, and in addition we define the vector $\hat{c}$ as the last column of $D$, which implies that the last element of $\hat{c}$ is zero. Using the definitions of $P$ and $Q$, we find

$$P\hat{r} = \hat{r} - \theta\nu\delta t\, \hat{c}, \tag{21}$$
$$Q\hat{r} = (1-\theta)\nu\delta t\, \hat{c}. \tag{22}$$

Application of $P^{-1}$ to both equations yields

$$\nu\delta t\, P^{-1}\hat{c} = (P^{-1}\hat{r} - \hat{r})/\theta, \tag{23}$$
$$P^{-1}Q\hat{r} = (1-\theta)\nu\delta t P^{-1}\hat{c}, \tag{24}$$

and these two equations imply

$$P^{-1}Q\hat{r} = \lambda(\hat{r} - P^{-1}\hat{r}) = \lambda(\hat{r} - \hat{\phi}^e), \tag{25}$$

where Eq. (13) has been used for the last equality. As a consequence,

$$A\hat{r} = (I + CR^{-1}J)P^{-1}Q\hat{r} = \lambda(I + CR^{-1}J)(\hat{r} - \hat{\phi}^e). \tag{26}$$

Equations (14) and (18) imply

$$CR^{-1}J\hat{\phi}^e = C\hat{v}^e = -\frac{1}{d^T \hat{v}^e}(\hat{\phi}^e d^T)v^e = -\frac{1}{d^T \hat{v}^e}\hat{\phi}^e(d^T v^e) = -\hat{\phi}^e. \tag{27}$$

In addition, since the last column in $J$ is zero, $J\hat{r} = 0$. Substitution of these properties into Eq. (26) yields

$$A\hat{r} = \lambda(\hat{r} - \hat{\phi}^e - CR^{-1}J\hat{\phi}^e) = \lambda(\hat{r} - \hat{\phi}^e + \hat{\phi}^e) = \lambda\hat{r}, \tag{28}$$

which proves the theorem.

All eigenvalues of matrix $A$ have been computed with Matlab for different values of $M$ and different values of $\theta$. It was found that $\hat{r}_1$ is the only eigenvector for $\lambda$, and that the absolute values of all other eigenvalues are less than 1. Similarly, the $\theta$-method applied to the odd analog of Eqs. (5-7) appears to have the same eigenvalue $\lambda$, and then the corresponding eigenvector corresponds to the highest odd Chebyshev mode present. Thus in the general problem with even and odd modes, the multiplicity of the eigenvalue $\lambda$ equals 2; the two corresponding eigenvectors are the last two Chebyshev modes.

# References

[1] A.W. Vreman and J.G.M. Kuerten, Statistics of spatial derivatives of velocity and pressure in turbulent channel flow, Phys. Fluids **26** (2014) 085103.

[2] P.R. Spalart, R.D. Moser, and M.M. Rogers, Spectral methods for the Navier-Stokes equations with one infinite and two periodic directions, *J. Comp. Phys.* **96** (1991) 297-324.

[3] D. Krasnov, M. Rossi, O. Zikanov, and T. Boeck, Optimal growth and transition to turbulence in turbulent channel flow with spanwise magnetic field, J. Fluid Mech. **596** (2008) 73-101.

[4] J. Kim, P. Moin, and R. Moser, Turbulence statistics in fully developed channel flow at low Reynolds number, *J. Fluid Mech.* **177** (1987) 133-166.

[5] R.D. Moser, J. Kim, and N.N. Mansour, Direct numerical simulations of turbulent channel flow up to $Re_\tau = 590$, *Phys. Fluids* **11** (1999) 943-945.

[6] J.C. del Álamo and J. Jiménez, Spectra of the very large anisotropic scales in turbulent channels, *Phys. Fluids* **15** (2003) L41-43.

[7] S. Hoyas and J. Jiménez, Scaling of the velocity fluctuations in turbulent channels up to $Re_\tau = 2003$, *Phys. Fluids* **18** (2006) 011702.

[8] S. Hoyas and J. Jiménez, Reynolds number effects on the Reynolds-stress budgets in turbulent channels, *Phys. Fluids* **20** (2008) 101511.

[9] T. Boeck, D. Krasnov, and J. Schumacher, Statistics of velocity gradients in wall-bounded shear flow turbulence, Phys. D **239** (2010) 1258-1263.

[10] P.E. Hamlington, D. Krasnov, T. Boeck, and J. Schumacher, Local dissipation scales and energy dissipation-rate moments in channel flow, J. Fluid Mech. **701** (2012) 419-429.

[11] J.G.M. Kuerten, C.W.M. van der Geld, and B.J. Geurts, Turbulence modification and heat transfer enhancement by inertial particles in turbulent channel flow, *Phys. Fluids* **23** (2011) 123301.

[12] B.J. Geurts and J.G.M. Kuerten, Ideal stochastic forcing for the motion of particles in large-eddy simulation extracted from direct numerical simulation of turbulent channel flow, *Phys. Fluids* **24** (2012) 081702.

[13] A.W. Vreman and J.G.M. Kuerten, Comparison of direct numerical simulation databases of turbulent channel flow at $Re_\tau = 180$, Phys. Fluids **26** (2014) 015102.

[14] L. Kleiser and U. Schumann, Treatment of Incompressibility and Boundary Conditions in 3-D Numerical Spectral Simulations of Plane Channel Flows, in: E.H. Hirschel (ed.), Proc. 3rd GAMM Conf. on Numerical Methods in Fluid Mechanics, Vieweg-Verlag, Braunschweig, 1980, pp. 165-173.

[15] S.A. Orszag, M. Israeli and M.O. Deville, Boundary conditions for incompressible flows, J. Sci. Comput. 1 (1986) 75-111.

[16] N.D. Sandham and L. Kleiser, The late stages of transition to turbulence in channel flow, *J. Fluid Mech.* **245** (1992) 319-348.

[17] Z.W. Hu, C.L. Morfey, and N.D. Sandham, Wall pressure and shear stress spectra from direct numerical simulations of channel flow up to Re$\tau$ = 1440, *AIAA Journal* **44** (2006) 1541-1549.

[18] D. Gottlieb and S.A. Orszag, Numerical analysis of spectral methods: Theory and applications, Capital City Press, Montpelier (Vermont, USA), 1977.

[19] C. Canuto, M.Y. Hussaini, A. Quarteroni, T.A. Zang, Spectral methods: Fundamentals in single domains, Springer, Berlin, 2006.

[20] N.N. Mansour, J. Kim, and P. Moin, Reynolds-stress and dissipation-rate budgets in turbulent channel flow, *J. Fluid Mech.* **194** (1988) 15-44.

[21] R.A. Antonia, J. Kim, Low-Reynolds-number effects on near-wall turbulence, *J. Fluid Mech.* **276** (1994) 61-80.

[22] J.J. Gorski, The enstrophy equation budget of bounded turbulent shear flows, Phys. Fluids **6** (1994) 1397-1399.

[23] F. Durst and K.N. Beronov, On the difficulties in resolving the viscous sublayer in wall-bounded turbulence, in Direct and Large-Eddy Simulation V, edited by R. Friedrich, B.J. Geurts, and O. Metais (Kluwer Academic, 2004), pp. 117-124.

[24] P. Lenaers, Q. Li, G. Brethouwer, P. Schlatter, and R. Örlü, Rare backflow and extreme wall-normal velocity fluctuations in near-wall turbulence, Phys. Fluids **24** (2012) 035110.